Supplementary information

Two-Step Templating Strategy Enabled 20.70% Efficiency Layer-by-Layer Organic Solar Cells

Siqi Huang,[a] Min Deng,[a,*] Xilin Lai,[a] Tao Chen,[a] Xingsong Bao,[a] Jun Liao,[a] Junyi Li,[a] Junying Wang,[a] Chentong Liao,[a] and Qiang Peng[a,b,*]

[a]College of Materials and Chemistry & Chemical Engineering, Chengdu University of Technology, Chengdu 610059, P. R. China. E-mail: mindeng@cdut.edu.cn; qiangpeng@scu.edu.cn

[b]School of Chemical Engineering and State Key Laboratory of Advanced Polymer Materials, Sichuan University, Chengdu 610065, P. R. China. E-mail: qiangpeng@scu.edu.cn

1. Materials and Methods

Materials: D18 and L8-BO were purchased from Solarmer Material Inc. 1,4-Diiodobenzene (DIB) were purchased from Tansoole. Poly(3,4-ethylenedioxythiophene):poly(styrenesulfonate) (PEDOT:PSS) were purchased from eflexPV Inc. PNDIT-F3N were purchased from Derthon Optoelectronics Materials Science Technology Co., LTD. Monomers BTP-8, 10-IC*m*Br[1] and BDD-$SnMe_3$[2] were synthesized according to previously reported procedures. All the other chemicals were purchased from Aladdin, Adamas, Sigma-Aldrich and Alfa Asear Chemical Co., and used without further purification. All solvents were freshly distilled immediately prior to use.

Synthesis of compound PBTP-BDD: In a round bottom flask, BTP-8, 10-IC*m*Br (100.00 mg, 0.0535 mmol), BDD-$SnMe_3$ (50.08 mg, 0.0535 mmol), $Pd_2(dba)_3$ (0.97 mg, 0.00106 mmol) and P(*o*-tolyl)$_3$ (1.30 mg, 0.00426 mmol) were dissolved in ultra-dry toluene (2.0 mL). The mixture was deoxygenated with nitrogen for three times and stirred at 115 °C for 30 mins. After cooling to room temperature, the mixture was dropped into methanol (500 mL) and filtered. The collected crude product was Soxhlet extracted with methanol, *n*-hexane, dichloromethane and chloroform. Finally, the chloroform fraction was concentrated and dropped into methanol (200 mL), after filtered and dried under vacuum to obtain PBTP-BDD as black solid (109.89 mg, 88.57%). M_w = 25817, M_n = 13566, *PDI* = 1.90.

Synthesis of compound PBTP-BDD-LW: In a round bottom flask, BTP-8, 10-IC*m*Br (100.00 mg, 0.0535 mmol), BDD-$SnMe_3$ (50.08 mg, 0.0535 mmol), $Pd_2(dba)_3$ (0.97 mg, 0.00106 mmol) and P(*o*-tolyl)$_3$ (1.30 mg, 0.00426 mmol) were dissolved in ultra-dry toluene (2.0 mL). The mixture was deoxygenated with nitrogen for three times and stirred at 115 °C for 20 mins. After cooling to room temperature, the mixture was dropped into methanol (500 mL) and filtered. The collected crude product was Soxhlet extracted with methanol, *n*-hexane, dichloromethane and chloroform. Finally, the chloroform fraction was concentrated and dropped into methanol (200 mL), after filtered and dried under vacuum to obtain PBTP-BDD as black solid (105.92 mg,

85.37%). M_w = 11731, M_n = 7059, *PDI* = 1.66.

Synthesis of compound PBTP-BDD-HW: In a round bottom flask, BTP-8, 10-IC*m*Br (100.00 mg, 0.0535 mmol), BDD-$SnMe_3$ (50.08 mg, 0.0535 mmol), $Pd_2(dba)_3$ (0.97 mg, 0.00106 mmol) and P(*o*-tolyl)$_3$ (1.30 mg, 0.00426 mmol) were dissolved in ultra-dry toluene (2.0 mL). The mixture was deoxygenated with nitrogen for three times and stirred at 115 ^oC for 50 mins. After cooling to room temperature, the mixture was dropped into methanol (500 mL) and filtered. The collected crude product was Soxhlet extracted with methanol, *n*-hexane, dichloromethane and chloroform. Finally, the chloroform fraction was concentrated and dropped into methanol (200 mL), after filtered and dried under vacuum to obtain PBTP-BDD as black solid (110.72 mg, 89.24%). M_w = 35420, M_n = 21251, *PDI* = 1.67.

2. Material characterizations

Density functional theory (DFT) was performed using Gaussian 16 A.03 program package. Optimized structures of PBTP-BDD were calculated at the B3LYP/631G(d, p) level. UV-vis spectra were obtained on a Hitachi U2910 spectrophotometer. Femtosecond transient absorption spectroscopy (fs-TAS) was conducted using a commercial Helios setup from Ultrafast Systems with a Ti:sapphire regenerative amplified laser system (Coherent Libra) delivered laser pulses at 780 nm (100 fs, 1 kHz). The probe beam was generated by focusing part of the fundamental femtosecond laser beam onto a sapphire plate or Yttrium aluminum garnet plate for visible (vis) and near-IR (NIR) spectral windows, respectively. TA results in this work are presented in the unit of ΔOD, negative features can reflect ground-state bleaching (GSB) or stimulated emission (SE), a positive signal is an excited-state absorption (ESA). During TA measurements, the samples were kept in nitrogen to avoid photodegradation. The pump fluence was kept at < 5 μJ cm^{-2} to minimize the exciton-exciton annihilation effect. GIWAXS measurements were performed on a Xenocs X-ray Small-angle Scatterer (Xeuss 2.0) with the Pilatus 3R 300K detector. AFM images were obtained by using a Bruker Nano IR3 atomic microscope in tapping mode. Transient photovoltage (TPV), transient photocurrent (TPC) and photogenerated

charge extraction by linearly increasing voltage (photo-CELIV) mobilities data were obtained by the all-in-one characterization platform, Paios (Fluxim AG, Switzerland). Cyclic voltammetry (CV) measurements were performed on a CH1650D electrochemical workstation, equipped with a three-electrode cell consisting of a platinum working electrode, a saturated calomel electrode (SCE) as reference electrode and a platinum wire counter electrode. CV measurements were carried out in anhydrous acetonitrile containing Bu_4NPF_6 (0.1 M) as a supporting electrolyte under an argon atmosphere at a scan rate of 50 mV s^{-1}. The potential of Ag/Ag^+ reference electrode was calibrated by using ferrocene/ferroncenium (Fc/Fc^+) as the redox couple. The HOMO and LUMO levels were calculated according to the formula, $E_{HOMO/LUMO}$ = -e ($E_{onset,ox/red}$-$E_{Fc/Fc+}$ + 4.30) .Surface energy characterization: Contact angle measurements were performed (at room temperature) on a Drop Shape Analyzer (DSA100) in the static mode. The surface free energy of each film was calculated through fitting. Specifically, the contact angle, averaged from the left and right angles of a sessile drop, was measured using the tangential method in the software. Deionized water and diiodomethane (1.5 μL) were dropped onto SiO_2 wafers with the neat film, and the droplet was photographed after reaching equilibrium at the gas-liquid-solid interface. The contact angle was fixed within a standard deviation of ± 1°. The Flory-Huggins interaction parameter was calculated using the relation, $\chi = \kappa(\sqrt{\gamma_A} - \sqrt{\gamma_B})^2$.

3. Fabrication and characterization of organic solar cells

3.1 Fabrication of organic solar cells devices

Cleaning of indium tin oxide (ITO) conductive glass: Clean the glass with detergent, deionized water, ethanol and acetone. Then dry and clean the ITO conductive glass with high-purity nitrogen gas to ensure that there is no liquid residue on the surface. Finally, treat the surface with ultraviolet ozone for 20 mins to further purify the surface and enhance its adhesion. After UV-ozone treatment, a PEDOT:PSS layer (~ 30 nm) was spin-coated on ITO substrate at 5000 rpm for 30 s, and baked in air at 150 °C for 15 min, then transferred to a glove box. The D18 (5 mg mL^{-1} in chloroform) solution or a mixed solution of D18 and 5% weight ratio of PBTP-BDD, PBTP-BDD-LW or PBTP-

BDD-HW was spin-coated onto the substrates at 3000 rpm for 30 s to form an underlying donor layer with a thickness of approximately 60 nm. Then, 30 uL of chloroform solvent was spin-coated on above donor layer at 3000 rpm for 30 s. This step did not involve thermal annealing. Finally, the L8-BO solution (7 mg mL^{-1} CF, 50 wt% DIB (w/w)) was then coated onto the donor film by spinning at 3000 rpm for 30 s and annealed at 90 ^{o}C for 5 mins. Preparation of PNDIT-F3N: Accurately weigh PNDIT-F3N and dissolve it in a mixed solvent of methanol and glacial acetic acid (v/v = 200:1), strictly controlling the concentration at 0.8 mg mL-1. Stir at room temperature for 30 mins to ensure complete dissolution. The evaporation process: Finally, the standardized device with effective area of 4.00 mm^2 and thickness of 90 nm silver electrode was obtained by evaporating silver in high vacuum chamber of 1×10^{-5} Pa.

3.2 Fabrication of hole-only and electron-only devices

Hole-only and electron-only devices for SCLC measurements were fabricated with similar methods in architectures of ITO/PEDOT:PSS/active layer/Au and ITO/ZnO/active layer/PNDIT-F3N/Ag, respectively. The ZnO layer was fabricated using a sol-gel method, and gold electrodes were deposited by thermal evaporation in vacuum. All device fabrications were performed in an argon gas filled glove box except for the deposition of PEDOT:PSS and ZnO layers.

3.3 *I*-V characterization

The *J-V* characteristics of devices were recorded using a Keithley 2400 Source Measure Unit under AM1.5 G (100 mW cm^{-2}) irradiation generated by a SAN-EI XES-70S1 solar simulator in an argon gas filled glove box.

3.4 External quantum efficiency

The EQE responses from OSC devices were recorded on an Enlitech QE-R solar quantum efficiency testing system in air. OSC devices for EQE, charge generation and charge recombination evaluations were the top performing devices.

3.5 Carrier mobility measurements

Charge carrier mobilities were tested using the space charge limited current (SCLC) method on hole-only and electron-only devices. The *J*-V curves measured on hole-only and electron-only devices were fitted to $J = 9\varepsilon_0\varepsilon_r\mu V^2/8L^3$, where J is the current density,

L is the film thickness of the active layer, μ is the hole or electron mobility, ε_r is the relative dielectric constant of the transport medium, ε_0 is the permittivity of free space (8.85×10^{-12} F m^{-1}), V is the internal voltage in the device and $V = V_{appl} - V_{bi} - V_a$, where V_{appl} is the applied voltage to the device, V_{bi} is the built-in voltage and V_a is the voltage drop.

4. Supporting Figures

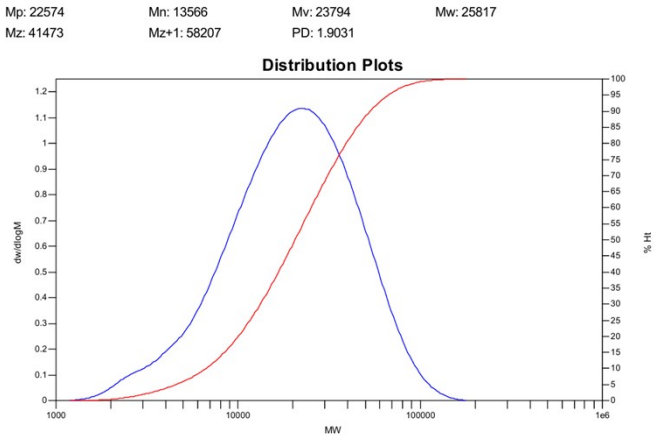

Fig. S1 HT-GPC diagram of PBTP-BDD.

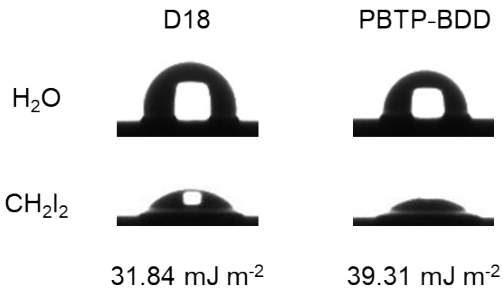

Fig. S2 Surface energy measurement for D18 and PBTP-BDD.

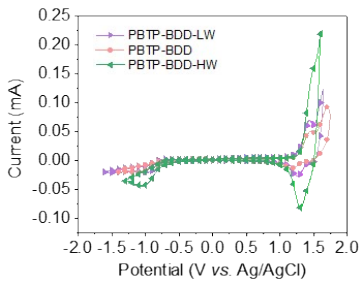

Fig. S3 CV curves of PBTP-BDD-LW, PBTP-BDD and PBTP-BDD-HW.

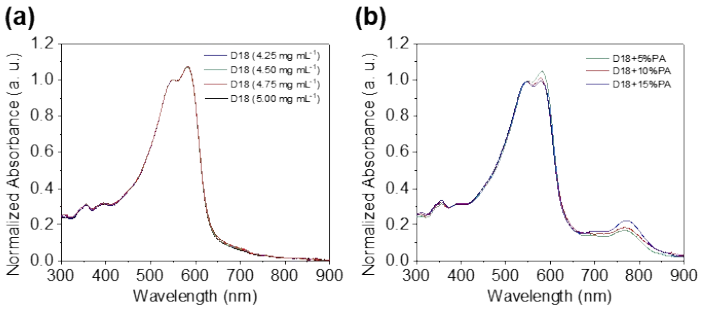

Fig. S4 (a, b) Normalized UV-vis-NIR absorption spectra of D18 with different concentration (a) and ratio of PA (b).

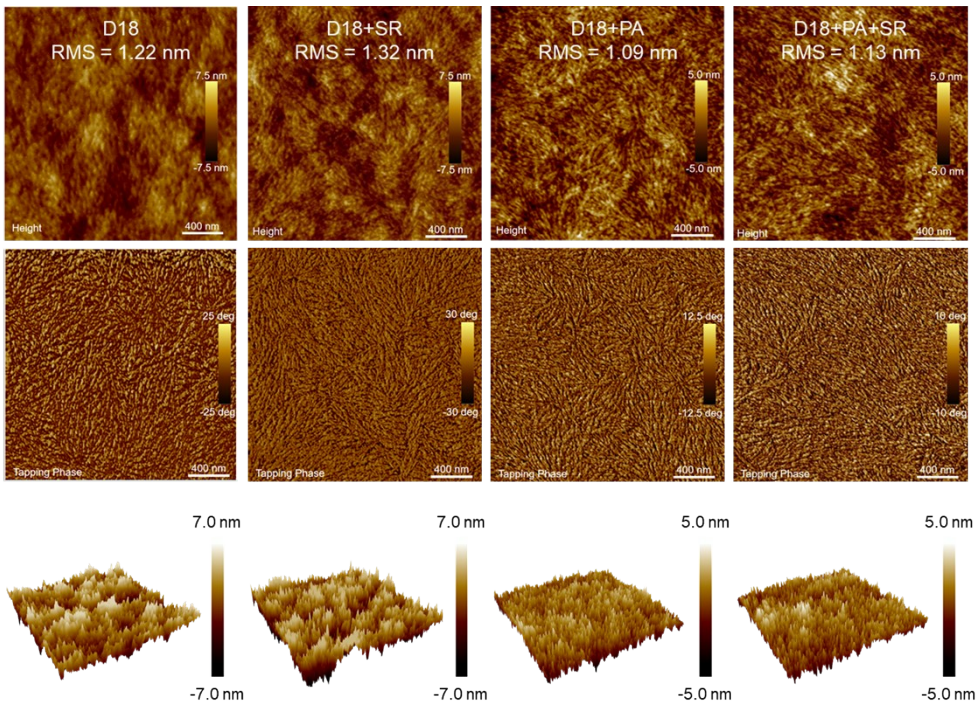

Fig. S5 AFM images of D18 treated with different post-processing.

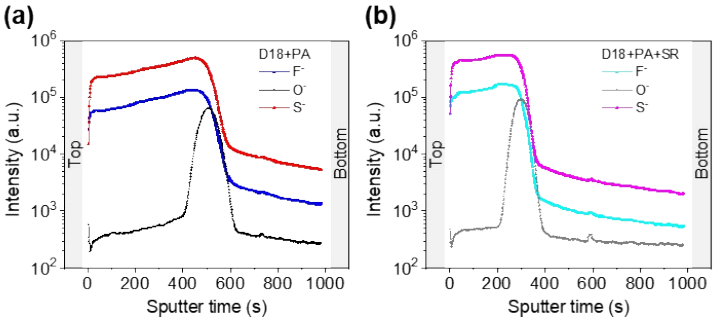

Fig. S6 The TOF-SIMS of D18+PA and D18+PA+SR films.

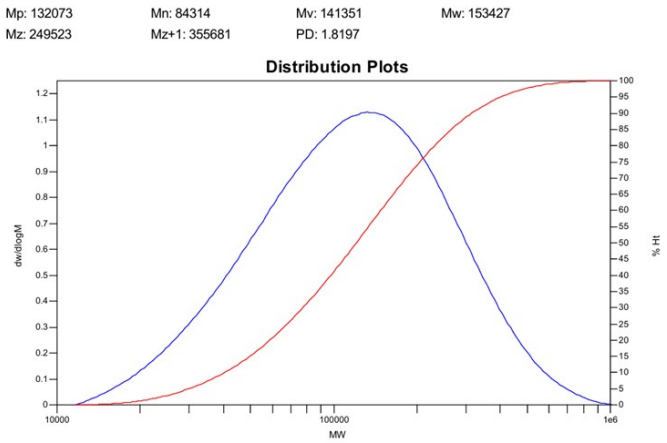

Fig. S7 HT-GPC diagram of medium molecular weight D18 (D18-M).

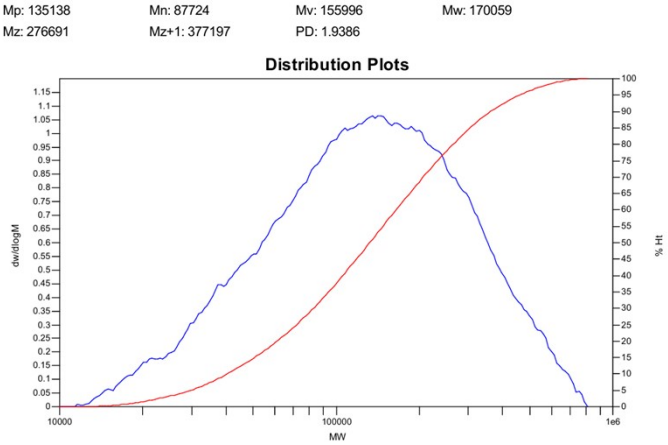

Fig. S8 HT-GPC diagram of the rinsed D18.

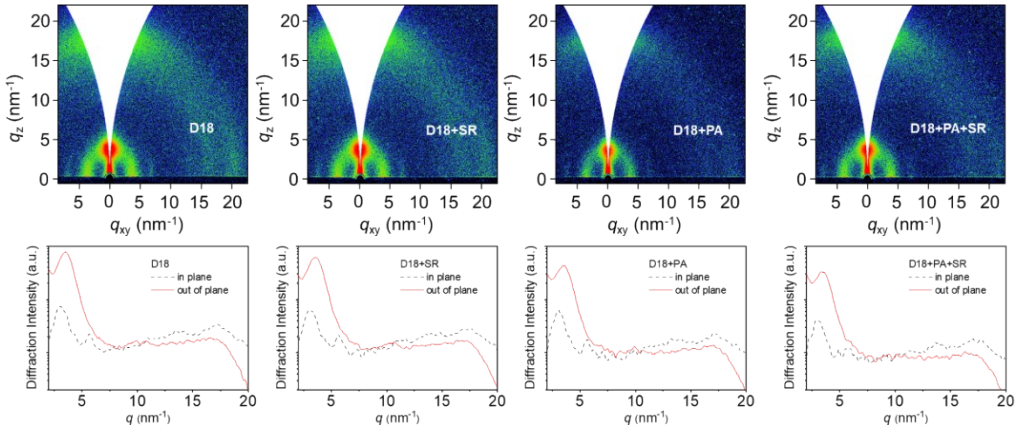

Fig. S9 2D GIWAXS images (top) and 1D line-cut profiles along the IP and OOP directions (bottom) of D18 and D18+PA before and after rinsing.

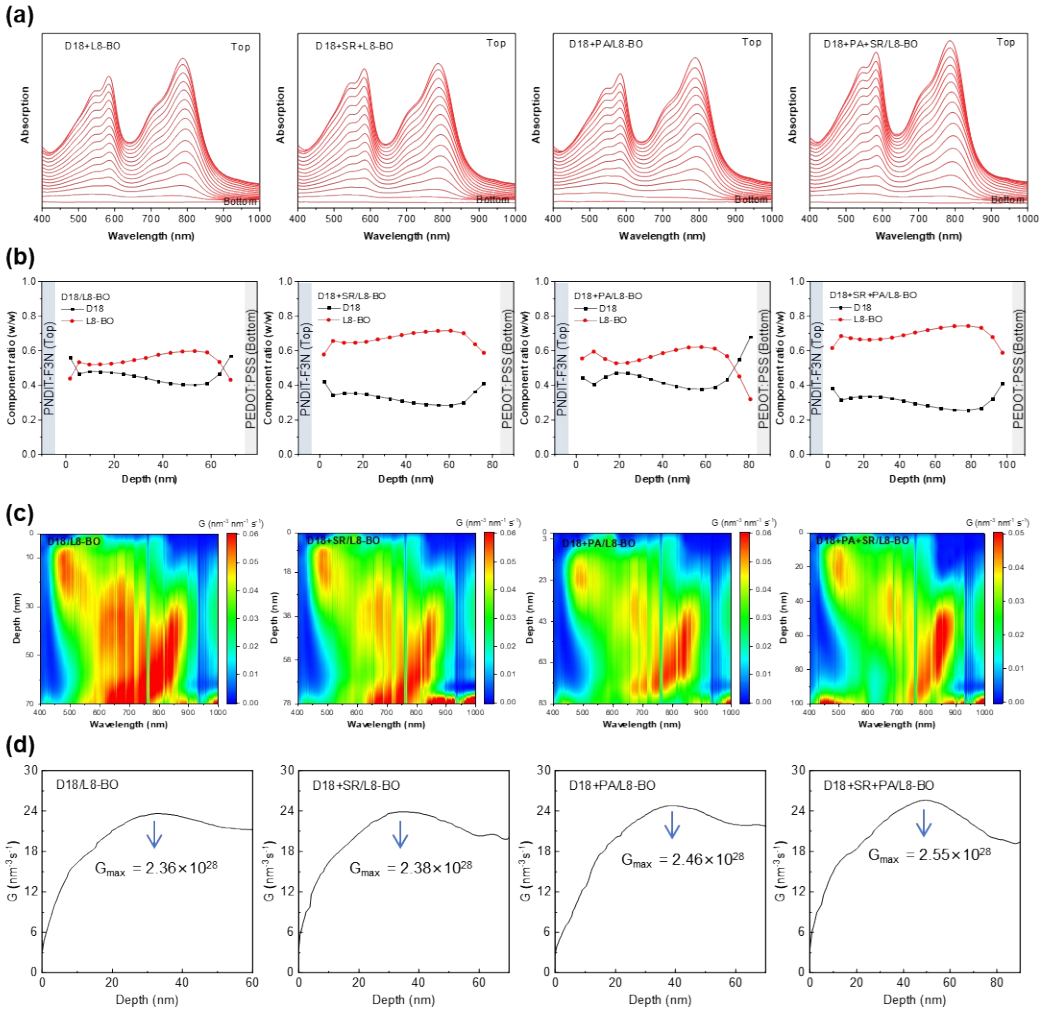

Fig. S10 (a) The FLAS characteristics of the D18/L8-BO films and those treated with rinsing strategy, plasticizating strategy and TST strategy. (b) The distribution ratio of D18 and L8-BO with the film thickness variation. (c) Exciton generation contours of the D18/L8-BO films and those treated with rinsing strategy, plasticizating strategy and TST strategy as numerically simulated from the FLAS. (d) The dependence of the simulated exciton generation rate on the film depth of D18/L8-BO films and those treated with rinsing strategy, plasticizating strategy and TST strategy.

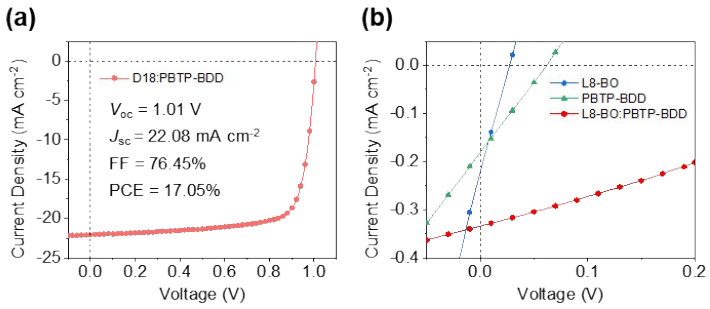

Fig. S11 (a) *J-V* curves of D18:PBTP-BDD devices. (b) *J-V* curves of acceptor-only devices.

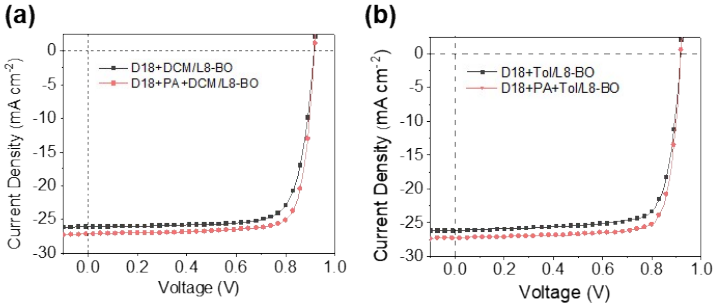

Fig. S12 (a-b) *J-V* curves of LBL OSCs with different rinsing solvents.

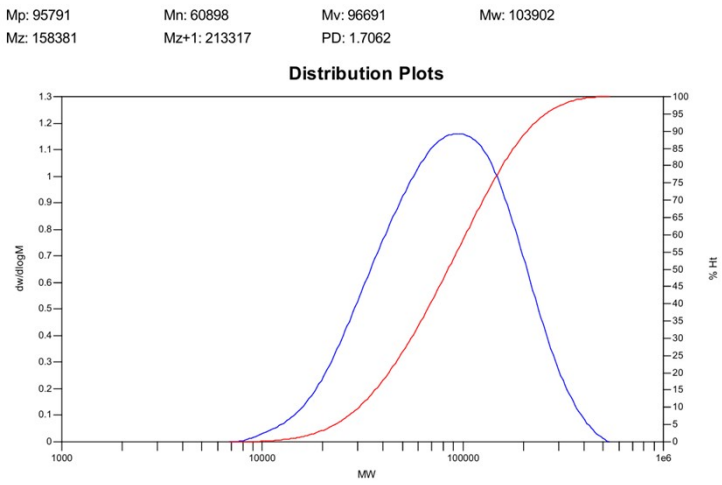

Fig. S13 HT-GPC diagram of low molecular weight D18 (D18-L).

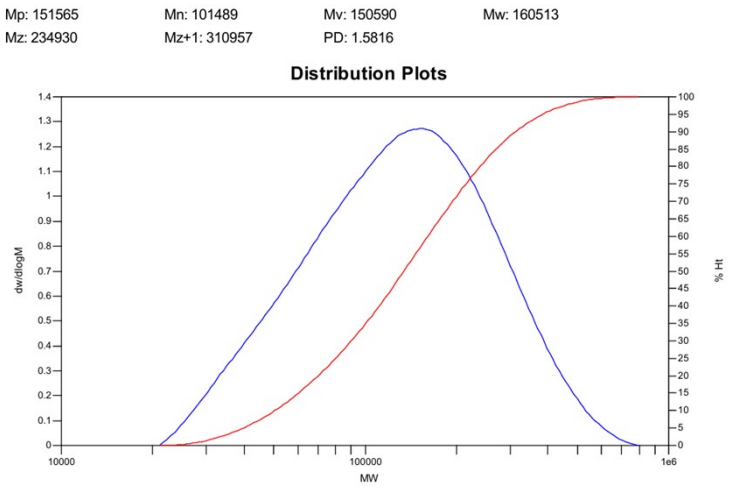

Fig. S14 HT-GPC diagram of high molecular weight D18 (D18-H).

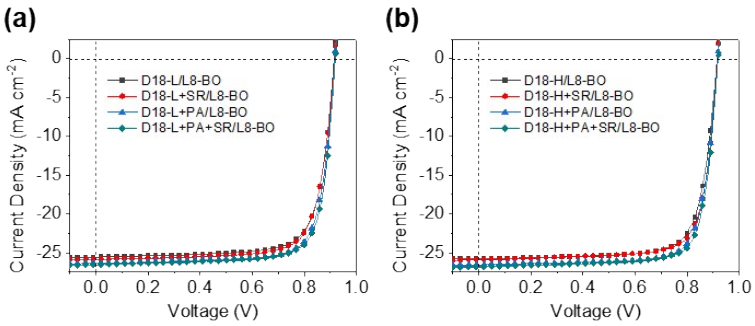

Fig. S15 (a) *J-V* curves of LBL OSCs based on low molecular weight D18. (b) *J-V* curves of LBL OSCs based on high molecular weight D18.

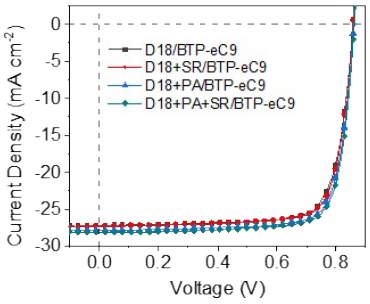

Fig. S16 *J-V* curves of D18:BTP-eC9 devices treated with of TST strategy.

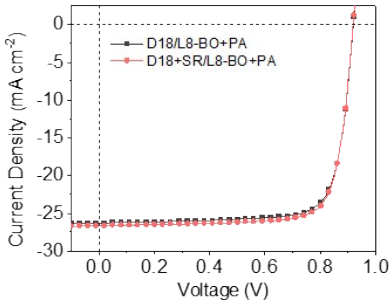

Fig. S17 *J-V* curves of LBL OSCs by adding plasticizer into top layer and combining with the rinsing strategy.

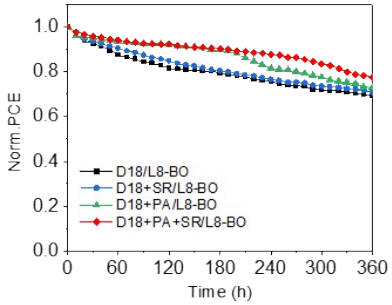

Fig. S18 Time-dependent normalized PCE under continuous light illumination for 360 h.

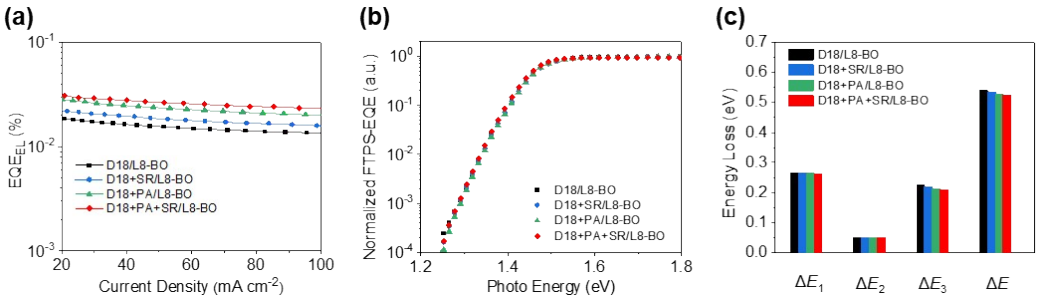

Fig. S19 (a) EQE_{EL} curves of LBL OSCs. (b) FTPS-EQE of LBL OSCs at the absorption onset. (c) Energy loss diagrams of LBL OSCs.

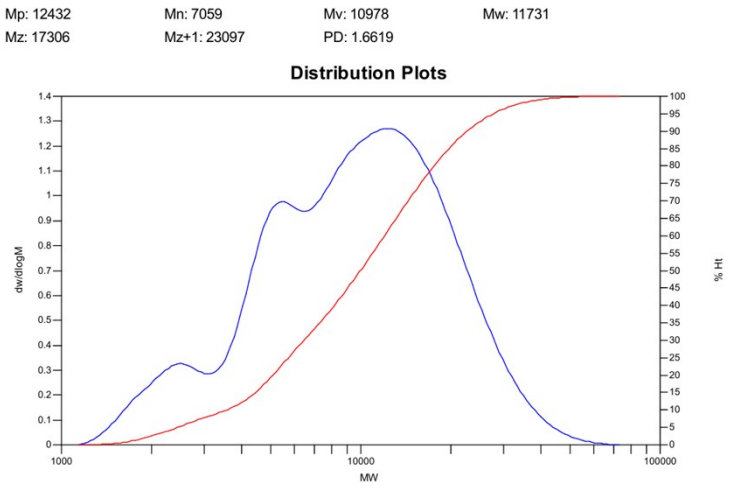

Fig. S20 HT-GPC diagram of PBTP-BDD-LW.

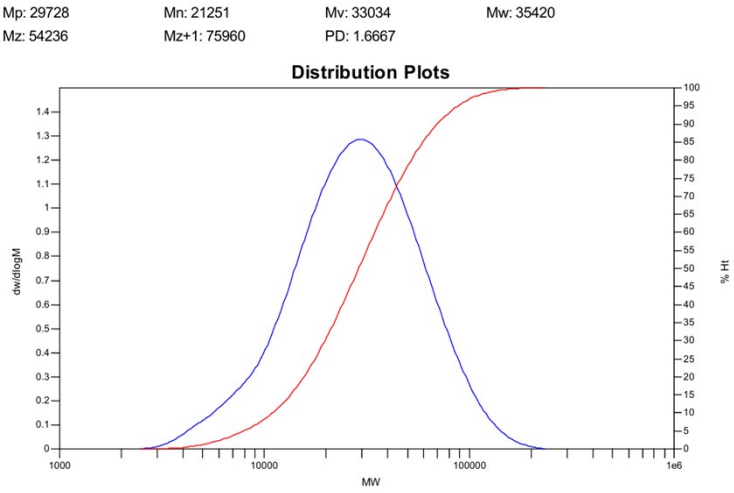

Fig. S21 HT-GPC diagram of PBTP-BDD-HW.

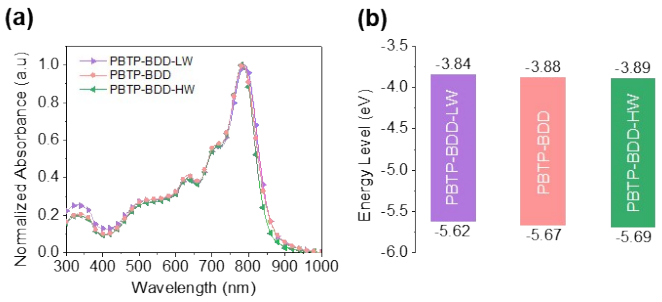

Fig. S22 (a, b) Normalized UV-vis-NIR absorption spectra (a) and energy level diagram (b) of PBTP-BDD-LW, PBTP-BDD and PBTP-BDD-HW.

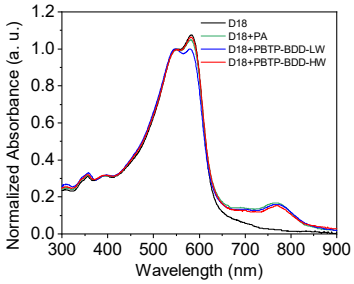

Fig. S23 Normalized UV-vis-NIR absorption spectra of D18 and D18 containing different molecular weight polymer plasticizer.

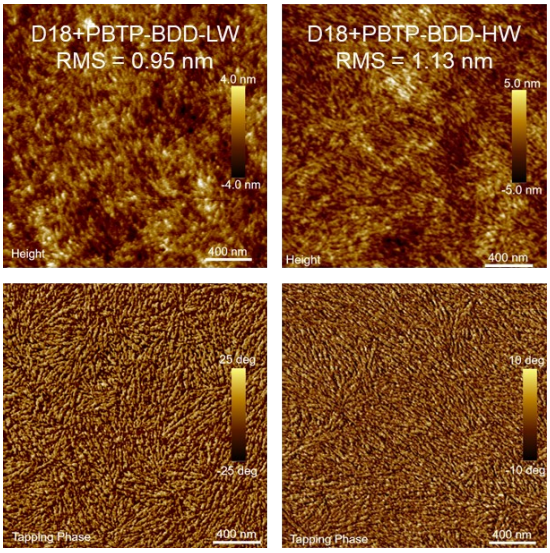

Fig. S24 AFM images of D18 containing PBTP-BDD-LW and PBTP-BDD-HW.

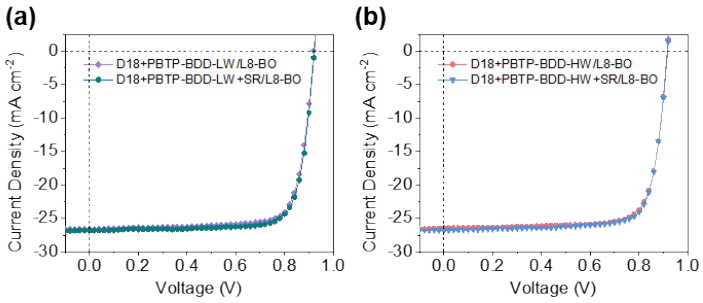

Fig. S25 (a-b) *J-V* curves of LBL OSCs based on PBTP-BDD-LW (a) and PBTP-BDD-HW (b).

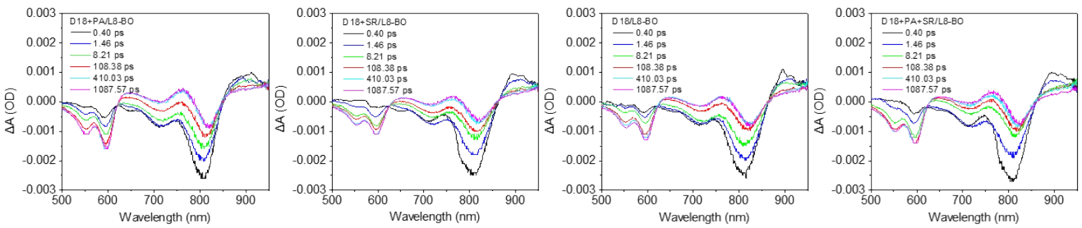

Fig. S26 TA spectra at different delay time.

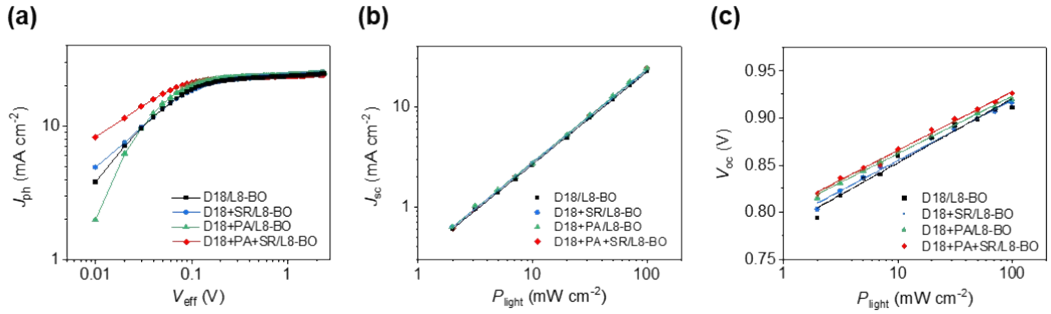

Fig. S27 (a) J_{ph} versus V_{eff} of the optimal LBL OSCs. (b, c) The plots of J_{sc} (b) and V_{oc} (c) versus P_{light} of the optimal LBL OSCs.

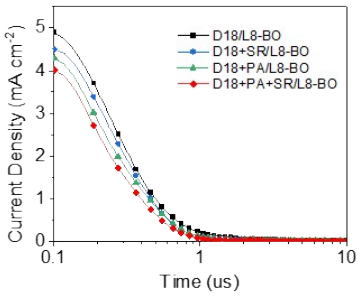

Fig. S28 DLTS curves of the blend films.

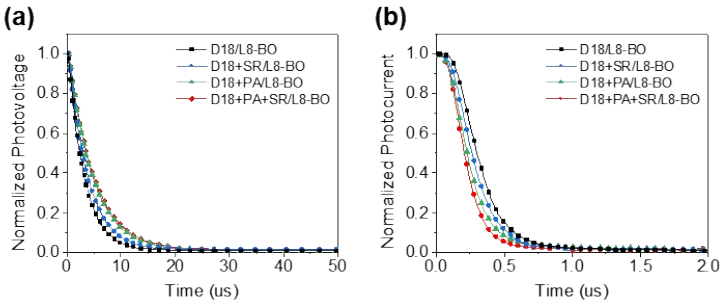

Fig. S29 TPC (a) and TPV (b) curves of LBL OSCs.

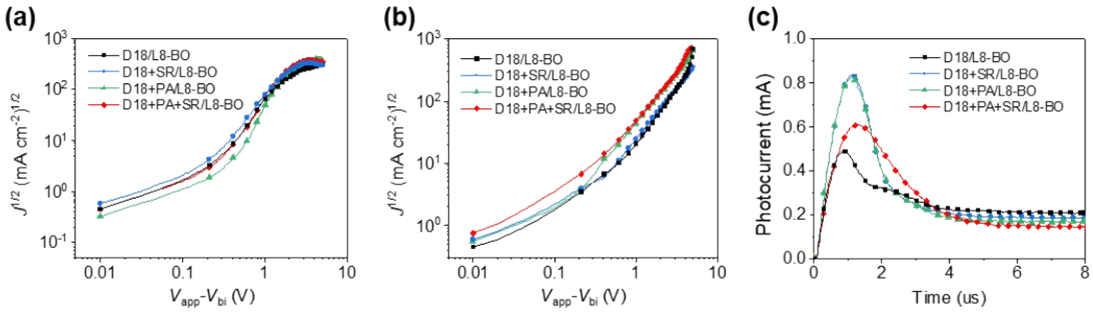

Fig. S30 (a, b) Hole mobility (a) and electron mobility (b) of the optimal LBL OSCs. (c) Photo-CELIV curves of the optimal LBL OSCs.

Table S1 Summarized parameters for the ordered structures.

films	lamellar stacking				π-π stacking			
	q (nm^{-1})	d (nm)	FWHM (nm^{-1})	CCL (nm)	q (nm^{-1})	d (nm)	FWHM (nm^{-1})	CCL (nm)
D18	3.12	2.01	0.71	7.88	17.26	0.36	1.80	3.10
D18+SR	3.14	2.00	0.69	8.11	17.28	0.36	1.72	3.25
D18+PA	3.08	2.04	0.80	6.99	17.15	0.37	2.28	2.45
D18+PA+SR	3.09	2.03	0.76	7.36	17.19	0.37	2.00	2.79
D18/L8-BO	3.15	1.99	0.77	7.27	17.34	0.36	-	-
D18+SR/L8-BO	3.17	1.98	0.76	7.36	17.36	0.36	-	-
D18+PA/L8-BO	3.19	1.97	0.73	7.67	17.42	0.36	-	-
D18+PA+SR/L8-BO	3.20	1.96	0.74	7.77	17.45	0.36	-	-

Table S2 *J-V* data of LBL OSCs with different rinsing solvents.

active layer	V_{oc} (V)	J_{sc} (mA cm^{-2})	FF (%)	PCE (%)
D18+DCM/L8-BO	0.915	26.08	78.00	18.61
D18+PA+DCM/L8-BO	0.918	27.15	80.58	20.08
D18+Tol/L8-BO	0.916	26.16	78.12	18.72

D18+PA+Tol/L8-BO	0.919	27.25	80.71	20.21

Table S3 *J-V* data of LBL OSCs based on low molecular weight D18.

active layer	V_{oc} (V)	J_{sc} (mA cm^{-2})	FF (%)	PCE (%)
D18-L/L8-BO	0.915	25.57	76.87	17.98
D18-L+SR/L8-BO	0.916	25.88	77.00	18.25
D18-L+PA/L8-BO	0.918	26.36	78.45	18.98
D18-L+PA+SR/L8-BO	0.919	26.58	78.59	19.20

Table S4 *J-V* data of LBL OSCs based on high molecular weight D18.

active layer	V_{oc} (V)	J_{sc} (mA cm^{-2})	FF (%)	PCE (%)
D18-H/L8-BO	0.915	25.74	77.26	18.20
D18-H+SR/L8-BO	0.916	25.96	78.02	18.55
D18-H+PA/L8-BO	0.918	26.55	78.79	19.20
D18-H+PA+SR/L8-BO	0.919	26.85	79.11	19.52

Table S5 *J-V* data of D18:BTP-eC9 devices treated with of TST strategy.

active layer	V_{oc} (V)	J_{sc} (mA cm^{-2})	FF (%)	PCE (%)
D18/BTP-eC9	0.858	27.11	78.10%	18.17
D18+SR/BTP-eC9	0.859	27.33	78.36%	18.40
D18+PA/BTP-eC9	0.862	27.89	78.97%	18.99
D18+PA+SR/BTP-eC9	0.863	28.12	79.25%	19.23

Table S6 *J-V* data of LBL OSCs by adding plasticizer into top layer and combining with the rinsing strategy.

active layer	V_{oc} (V)	J_{sc} (mA cm^{-2})	FF (%)	PCE (%)
D18/L8-BO+PA	0.918	26.22	78.29	18.84
D18+SR/L8-BO+PA	0.919	26.59	78.72	19.24

Table S7 *J-V* data of LBL OSCs containing PBTP-BDD-LW.

active layer	V_{oc} (V)	J_{sc} (mA cm^{-2})	FF (%)	PCE (%)
D18+PBTP-BDD-LW/L8-BO	0.920	26.61	78.95	19.33
D18+PBTP-BDD-LW+SR/L8-BO	0.922	26.82	79.11	19.56

Table S8 *J-V* data of LBL OSCs containing PBTP-BDD-HW.

active layer	V_{oc} (V)	J_{sc} (mA cm^{-2})	FF (%)	PCE (%)
D18+PBTP-BDD-HW/L8-BO	0.916	26.45	78.73	19.07
D18+PBTP-BDD-HW+SR/L8-BO	0.917	26.78	78.95	19.39

Table S9 *J-V* data of thick-film OSCs based on D18/L8-BO films.

thickness (nm)	V_{oc} (V)	J_{sc} (mA cm^{-2})	FF (%)	PCE (%)
200	0.896	26.08	72.52	16.95
300	0.882	26.11	69.21	15.94

Table S10 *J-V* data of thick-film OSCs based on D18+PA+SR/L8-BO films.

thickness (nm)	V_{oc} (V)	J_{sc} (mA cm^{-2})	FF (%)	PCE (%)
200	0.905	27.60	76.81	19.19
300	0.890	27.66	73.46	18.08

References

1 H. Qin, S. Xia, D. Sun, Z. Wu, Y. Wang, Y. Ran, G. Lu, H. Y. Woo, B. Zhao, C. Gao, Y. Li, *J. Mater. Chem. C*, **2022**, *10*, 16397-16406.

2 H. Zhang, S. Zhang, K. Gao, F. Liu, H. Yao, B. Yang, C. He, T. P. Russell, J. Hou, *J. Mater. Chem. A*, **2017**, *5*, 10416-10423.